IEEE Photonics Journal
An IEEE Photonics Society Publication

Ultra-Wideband Signal Generation Based on a Silicon Segmented Mach-Zehnder Modulator

Volume 12, Number 6, December 2020

Gangqiang Zhou
Yuyao Guo
Liangjun Lu
Jianping Chen
Linjie Zhou

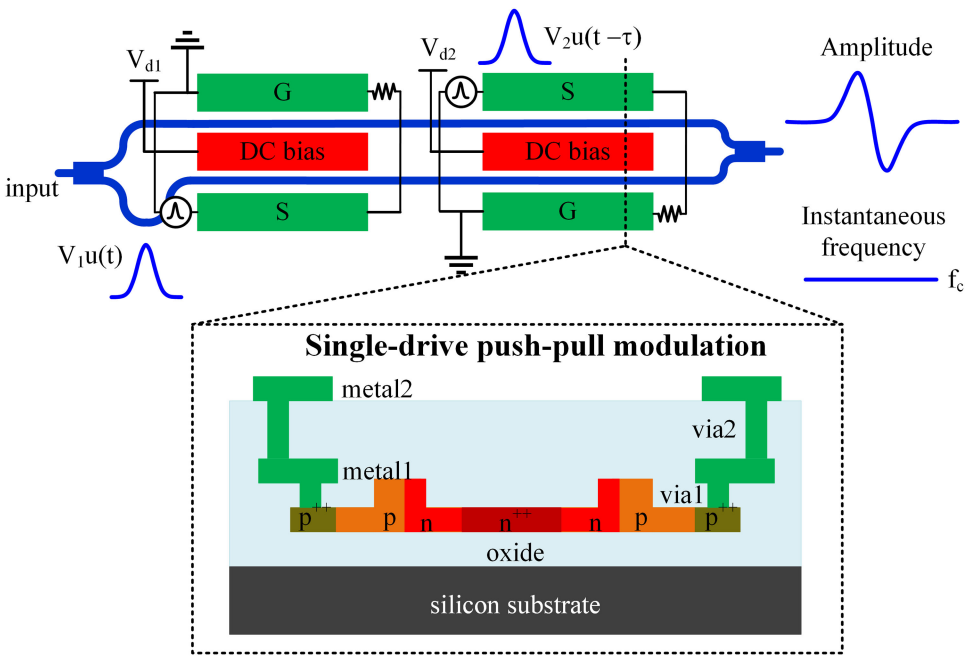

DOI: 10.1109/JPHOT.2020.3032967

Ultra-Wideband Signal Generation Based on a Silicon Segmented Mach-Zehnder Modulator

Gangqiang Zhou, Yuyao Guo, Liangjun Lu, Jianping Chen, and Linjie Zhou

State Key Laboratory of Advanced Optical Communication Systems and Networks, Shanghai Key Lab of Navigation and Location Services, Department of Electronic Engineering, Shanghai Jiao Tong University, Shanghai 200240, China

DOI:10.1109/JPHOT.2020.3032967

Manuscript received August 19, 2020; revised October 2, 2020; accepted October 19, 2020. Date of publication October 22, 2020; date of current version November 5, 2020. Corresponding author: Liangjun Lu (e-mail: luliangjun@sjtu.edu.cn).

Abstract: In this paper, we demonstrate a method to generate a low-chirp ultra-wideband pulse (UWB) signal based on a silicon single-drive push-pull segmented Mach-Zehnder modulator (SMZM). The concept is analyzed theoretically and demonstrated experimentally. We get positive monocycle pulses with different relative time delays between the two driving signals. The center frequency and fractional bandwidth of the generated positive monocycle pulse is 5.97 GHz and 161% with a relative time delay of 56 ps. By changing the operating point of the SMZM, we can get negative monocycle pulses. We modulate the UWB signals with on-off keying and pulse position formats by properly coding the driving signal. As far as we know, this is the first time to realize low-chirp UWB signals using only one silicon modulator. The successful generation of UWB signals poses a significant step in realizing a compact low-cost and low-chirp UWB generator on the silicon photonics platform.

Index Terms: Segmented Mach-Zehnder modulator, silicon modulator, UWB signal.

1. Introduction

Due to the high bit-rate, superior security, and low power consumption, an ultra-wideband (UWB) pulse signal is a good candidate for short-range and high-speed wireless communication systems [1], [2]. The UWB technology has been adopted in the products of Apple Inc. However, the transmission distance is usually short due to the low power spectral density (PSD). To increase the transmission distance, UWB over fiber (UWBoF) is proposed [3], [4]. Thus, an optical UWB signal is necessary for UWBoF. The UWB signals can be firstly generated in the electrical domain and then modulated onto an optical beam. This approach demands a high requirement for high-speed electrical driving systems. It is more beneficial to synthesize UWB signals directly in the optical domain. There are various methods to generate UWB signals in the optical domain [5]–[20]. One method is through phase modulation to intensity modulation conversion [6]–[11]. The conversion can be realized by many structures that work as frequency discriminators, for example, Bragg grating (BG) [6], Sagnac interferometer comb filter [7], asymmetric Mach-Zehnder interferometer [8], silicon micro-ring resonator (MR) [9], silicon micro-ring modulator (MRM) [10], silicon nitride (SiN) programmable photonic chip [11], and so on. Semiconductor optical amplifier (SOA) can also be used to produce UWB signals [12]–[14]. UWB signal generation based on cross-gain modulation

(XGM) in SOA was realized [12]. In [13], the UWB signal was generated based on cross-phase modulation of SOA. UWB signal generation utilizing gain saturation of SOA was also demonstrated in [14]. Usually, the generated UWB signal is chirped and easily distorted when it is transmitted in an optical fiber due to the chromatic dispersion (CD) of the optical fiber [6]–[14].

Systems that can generate UWB signals with zero chirps or low chirps have been developed [15]–[20], which could reduce the distortion caused by the fiber CD [17]. Intensity modulation and multiple wavelength laser sources have been used to realize UWB signals [15], [16]. However, the adoption of multiple lasers makes the system complicated and costly. Electrical UWB signals can be converted into the optical domain with a zero chirp, if it is modulated using a push-pull Mach-Zehnder modulator (MZM) [17]. However, it imposes a high requirement for electrical hardware as mentioned before. A polarization modulator (PolM) and a photonic microwave filter have been used to realize chirp-free UWB signals in the optical domain [18], [19]. Usually, this method requires a polarization-maintaining fiber (PMF). Besides, the PolM is hard to integrate on the silicon platform. Chirp-free UWB signals have been produced by using two cascaded individual $LiNbO_3$ MZM [20]. Two-phase shifters are needed to set the operating point of the two modulators. The optical loss is 6 dB (3-dB per modulator) as the operating point is set at the quadrature point.

Recently, integrated microwave photonics (IMWP) has developed rapidly because integration can greatly reduce system weight, volume, and complexity [21]. There are many material platforms for IMWP, for example silicon nitride (Si_3N_4) [22], indium phosphide (InP) [23], silicon-on-insulator (SOI) [24] and so on. IMWP based on SOI has drawn great interests due to its complementary metal-oxide-semiconductor (CMOS) compatibility and high integration density. In IMWP systems, the compact electro-optic modulator is a key enabling component. Silicon electro-optic modulators have been widely investigated [25]–[27], and employed in microwave signal generation and processing [28]–[32]. For example, a silicon phase modulator (PM) followed by a micro-disk resonator (MDR) and a photodiode (PD) has been used to realize a microwave filter [28] and an optoelectronic oscillator for microwave generation [29]. A silicon MRM [30] and cascaded silicon MZMs [31] have been used to generate frequency combs. A silicon MRM followed by an external modulator [32] has been used to generate phase-coded microwave signals. For UWB signal generation, a silicon MRM was used as a tunable discriminator to generate amplitude and phase-modulated UWB signals based on PM-IM conversion [10]. However, the system also needs an external phase modulator to realize phase modulation. Comparing with $LiNbO_3$ modulators [5]–[20], silicon modulators possess the key merits of small size and CMOS compatibility, leading to high integration density and low cost. It is thus worth exploring UWB signal generation based on silicon modulators. Fano resonances from a silicon micro-ring-assisted Mach-Zehnder modulator (MRAMZM) have been used to generate UWB signals, but they are highly chirped due to the direct modulation of the ring resonance wavelength [33].

In this paper, we report the generation of low-chirp UWB signals by using an integrated silicon segmented Mach-Zehnder modulator (SMZM). It should be noted that two simple Gaussian-like electrical pulses are used in our scheme instead of UWB electrical pulses to drive the modulator. In essence, the complexity of the RF driving signal is transferred to the modulator where the two-segment design greatly relaxes its requirement on the driving signal. The silicon SMZM was originally devised for pulse-amplitude-modulation (PAM) [34]. We have demonstrated that a silicon SMZM can be employed for phase-coded microwave signal generation [35]. In this work, we show that the SMZM can be used for UWB signal generation, and therefore it is different from the previous work [34], [35] in terms of function and application field. As far as we know, this is the first time to realize low-chirp UWB signals using only one segmented silicon modulator. Due to the nonlinear free-carrier dispersion (FCD) and free-carrier absorption (FCA) effects in silicon modulators and the finite interference extinction ratio of the Mach-Zehnder interferometer (MZI), there is a small amount of residual chirp. The successful generation of UWB signals poses a significant step in realizing a compact low-cost and low-chirp UWB generator on the silicon photonics platform. Both positive and negative monocycle UWB signals can be generated by properly setting the operating point of the SMZM.

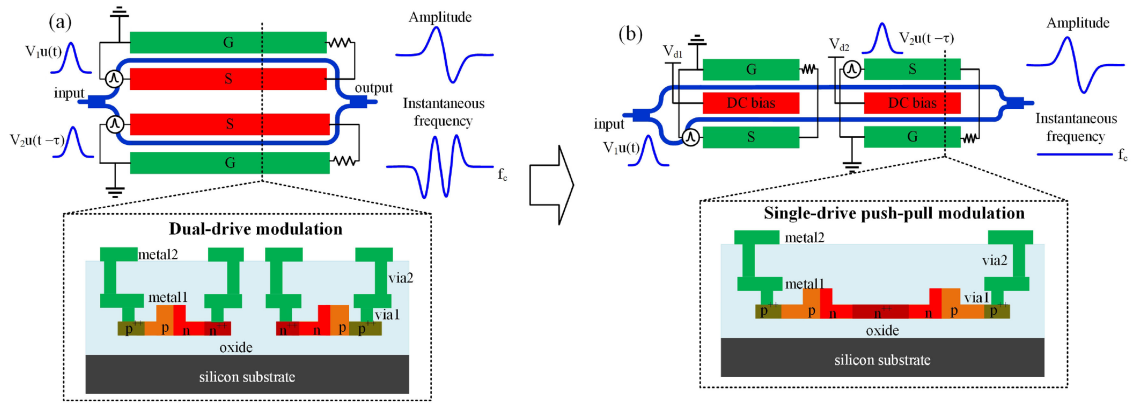

Fig. 1. UWB signal generation based on (a) the traditional dual-drive modulator and (b) the SMZM. The insets show the cross-section of the modulation arms. A constant instantaneous frequency is obtained for the SMZM.

2. Device Structure

A traditional method to generate the UWB signal in the optical domain is based on a dual-drive MZM [17], [36], as shown in Fig. 1(a). By applying two Gaussian pulses with a certain time delay on the two arms of the dual-drive modulator, a UWB signal is generated. However, in this method, the two Gaussian-like pulses are identical to each other and the phase difference of the two electrical pulses is not equal to π. It indicates that the dual-drive modulator does not work in the push-pull condition. Thus, the generated UWB signal is highly chirped, leading to signal distortion after transmission through a long fiber due to the CD [17]. Therefore, we propose a modified modulator structure with two segments of single-drive push-pull traveling-wave electrodes (TWEs) to generate low-chirp UWB signals, as shown in Fig. 1(b). Two Gaussian pulses are applied to the two segments, respectively. As the total length of the active arm in the SMZM is longer than that in the dual-drive modulator, the insertion loss is higher under the same PN junction design. However, as there is almost no phase modulation in the push-pull scheme, the instantaneous frequency of the generated signal is nearly constant, leading to low chirps. Compared to the dual-drive configuration, the single-drive one has a smaller capacitance as the PN junctions in the two arms are connected in series. This reduces the microwave transmission loss [37]. Besides, comparing with two cascaded MZMs, the optical loss of our device is 3 dB when the operating point is set at the quadrature point since the segmented Mach-Zehnder modulator is essentially realized from one MZI structure.

Fig. 2(a) shows the layout of the SMZM. The length of the TWEs is 2.3 mm for both segments. The MZI is an imbalanced structure with the arm length difference being 90 μm. Hence, the operating point of the modulator can be adjusted by changing the optical wavelength of the input light. As shown in the inset of Fig. 1(b), a pair of horizontal PN junctions are connected in series. The width and height of the rib waveguide are 500 nm and 220 nm, respectively. The slab height is 90 nm. To balance the insertion loss and the half-wave voltage, the optimized doping concentrations are chosen to be $\sim 5 \times 10^{17}$ cm^{-3} and $\sim 3 \times 10^{17}$ cm^{-3} for the n-doped and p-doped regions, respectively. The position of the PN junction is offset from the center of the rib waveguide to the n-doped side by 100 nm to maximize the modal overlap with the p-type region and get a higher modulation efficiency because silicon refractive index change is more sensitive to variation in hole concentration [38]. The distance between the heavily doped regions and the edge of the rib waveguide is 500 nm. To form good ohmic contacts, the doping concentrations of the n^{++}- and p^{++}-doped regions are increased to $\sim 1 \times 10^{20}$ cm^{-3}. The TWEs consist of two layers of aluminum metals. The widths of the signal and ground lines in metal1 are both 9 μm and the gap distance between them is 56 μm. The widths of the signal and ground lines in metal2 are both 60 μm and the gap distance between them is 20 μm. A direct current (DC) bias line is connected to the n^{++}-doping

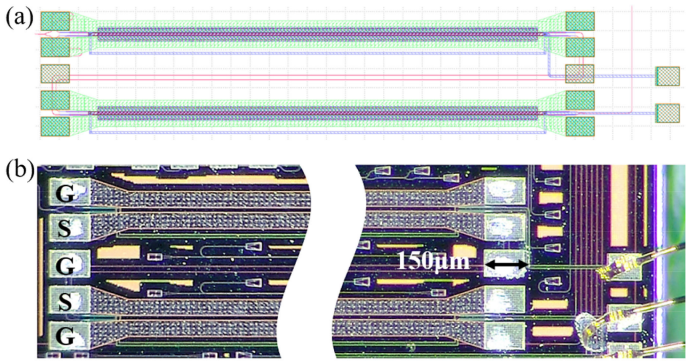

Fig. 2. (a) Layout of the SMZM. The two segments are aligned in parallel to facilitate the application of microwave signals. (b) Microscope image of the modulator after wire-bonding.

region to set the reverse bias condition of the PN junctions. Fig. 2(b) shows the microscope image of the fabricated device after wire-bonding the DC bias lines to a print circuit board (PCB). The device footprint is 2.9 mm $\times$ 0.7 mm.

3. Operating Principle

To generate the UWB pulses, two electrical Gaussian pulses, $S_1(t) = V_1 u(t)$ and $S_2(t) = V_2 u(t\text{-}\tau)$, are applied to the two TWEs, where V_1 and V_2 are the amplitudes of the Gaussian pulses, τ is the relative time delay between them, and $u(t)$ is the normalized Gaussian pulse. Assuming the input optical wave is $E_{\text{in}} = \exp(j2\pi f_c t)$, where f_c is the frequency of the optical wave, the output optical wave E_{out} can be expressed as:

$$E_{\text{out}}(t) = \frac{1}{2} E_{\text{in}} e^{j(\varphi_1+\varphi_2)} \left[e^{j(\theta_1-\theta_2)} + e^{j(-\theta_1+\theta_2+\Delta\theta)} \right] \tag{1}$$

where φ_1 and φ_2 are the phase shifts by the DC bias voltages V_{d1} and V_{d2} on the two segments, respectively, θ_1 and θ_2 are the phase modulations by $S_1(t)$ and $S_1(t)$, respectively, and $\Delta\theta$ is the phase difference between two arms. The phase shifts are given by

$$\varphi_1 = \pi V_{d1} / V_{\pi 1} \tag{2}$$

$$\varphi_2 = \pi V_{d2} / V_{\pi 2} \tag{3}$$

and the phase modulations are given by

$$\theta_1 = \pi V_1 u(t) / (2V_{\pi 1}) \tag{4}$$

$$\theta_2 = \pi V_2 u(t-\tau) / (2V_{\pi 2}) \tag{5}$$

where $V_{\pi 1}$ and $V_{\pi 2}$ are the half-wave voltages of the two segments, respectively. It should be noted that we assume linear phase modulation and no extra loss induced for simplicity. Because the two PN junctions are connected in series, the RF voltage drop on each PN junction is half of the applied voltage, resulting in a factor of 1/2 in Eq. (4) and Eq. (5). When the modulated signal is detected by a photodiode (PD), the generated photocurrent is

$$\begin{aligned} i_{\text{out}} &\propto E_{\text{out}}(t)\, E_{\text{out}}(t)^* \\ &\propto \frac{1}{4} \left[2 + e^{j(2\theta_1-2\theta_2-\Delta\theta)} + e^{j(-2\theta_1+2\theta_2+\Delta\theta)} \right] \\ &\propto \frac{1}{2} \left[1 + \cos(2\theta_1 - 2\theta_2 - \Delta\theta) \right] \end{aligned} \tag{6}$$

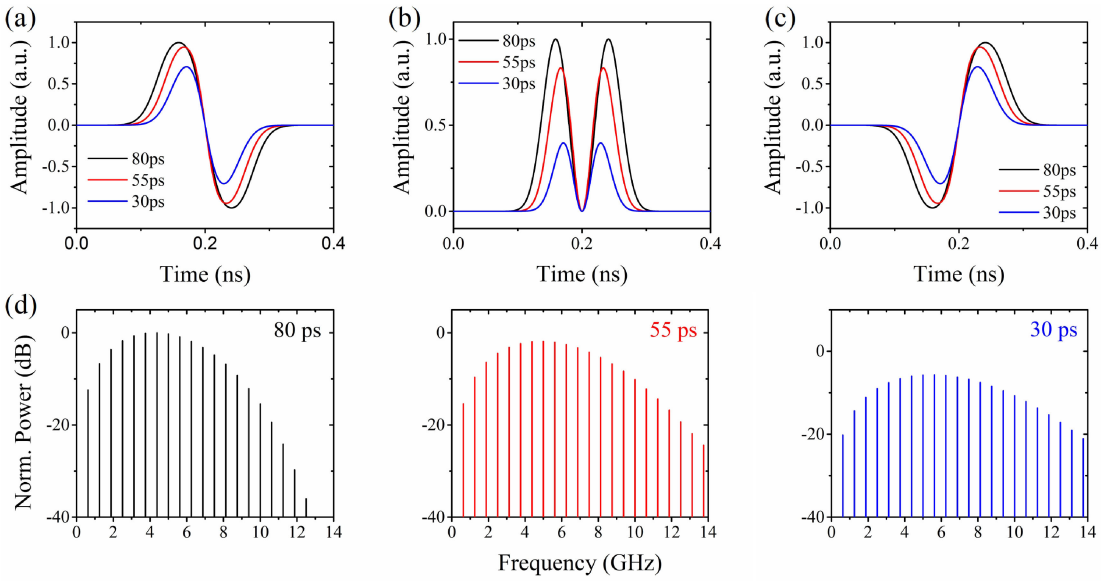

Fig. 3. Simulated UWB signal generation when the phase difference between two arms is (a) $-\pi/2$, (b) π, and (c) $\pi/2$. (d) Corresponding spectra of the waveform in (a).

Substitute Eq. (4) and Eq. (5) into Eq. (6), we have

$$i_{\text{out}} \propto \frac{1}{2}\left\{1+\cos\left[\frac{V_1 u(t)}{V_{\pi 1}}-\frac{V_2 u(t-\tau)}{V_{\pi 2}}-\Delta\theta\right]\right\} \tag{7}$$

Assuming $V_1 = V_2 = V$ and $V_{\pi 1} = V_{\pi 2} = V_\pi$, and $\Delta\theta = -\pi/2$, then we have

$$i_{\text{out}} \propto \frac{1}{2}\left\{1-\sin\left[\frac{V u(t)}{V_\pi}-\frac{V u(t-\tau)}{V_\pi}\right]\right\} \tag{8}$$

Under small-signal modulation, Eq. (8) is approximated as

$$i_{\text{out}} \propto \frac{1}{2}\left\{1-\frac{V}{V_\pi}[u(t)-u(t-\tau)]\right\} \tag{9}$$

If τ is sufficiently small, Eq. (9) can be expressed as [17]:

$$i_{\text{out}} \propto \frac{1}{2}\left\{1-\frac{V}{V_\pi}\tau u(t)'\right\} \tag{10}$$

Neglecting the DC term of the output current, the device can be regarded as a first-order differentiator. Thus, when $V > 0$, a negative monocycle pulse is generated. When $V < 0$, a positive monocycle pulse is generated. Here, we define a monocycle pulse with a leading peak followed by a trough as a positive one and a leading trough followed by a peak as a negative one. On the other hand, if $\Delta\theta = \pi/2$, the output current of the PD can be expressed as:

$$i_{\text{out}} \propto \frac{1}{2}\left\{1+\frac{V}{V_\pi}\tau u(t)'\right\} \tag{11}$$

Thus, when $V > 0$, a positive monocycle pulse is generated. When $V < 0$, a negative monocycle pulse is generated. Therefore, by changing the operating point of the SMZM, we can get both positive and negative monocycle pulses. Figs. 3(a), 3(b), and 3(c) show the simulated results when $V < 0$ and the phase difference between two arms are $-\pi/2$, π, and $\pi/2$, respectively. The relative time delay between two electrical pulses varies from 30ps to 80ps. Fig. 3(d) shows the corresponding spectra of the waveform in Fig. 3(a). The UWB pulses are quite dependent on the

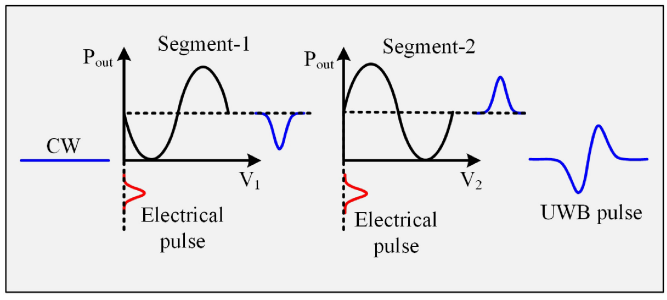

Fig. 4. Operating principle of the UWB signal generation based on the SMZM when $V > 0$ and $\Delta\theta = -\pi/2$. CW: input continuous-wave laser light.

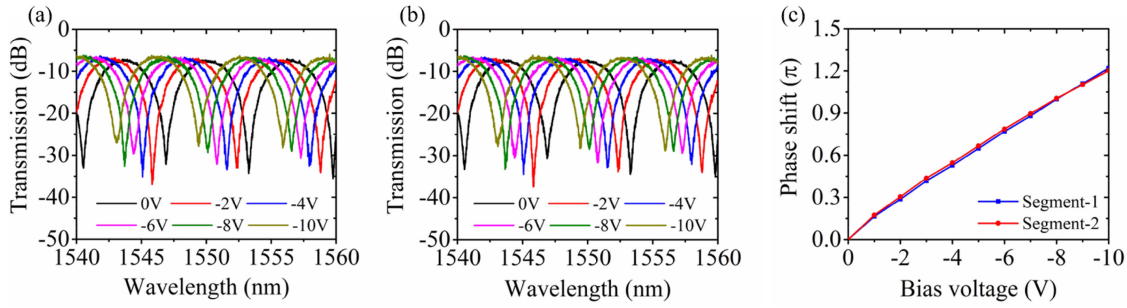

Fig. 5. Transmission spectra of the SMZM with bias voltages applied on one PN junction of (a) segment-1 and (b) segment-2. (c) Extracted phase shift as a function of bias voltage.

operating point of the SMZM. By changing the operating point, we could change the polarity of the generated UWB signal. Time delays between the Gaussian-like pulses also affect the generated UWB signal. With a shorter time delay, the amplitude of the generated UWB signal decreases, the FWHM of the peak and trough decreases, the center frequency of the UWB pulses increases, and the 10-dB bandwidth becomes broader.

The operating principle can be understood from Fig. 4 when $V > 0$. The operating point of the modulator is set to the quadrature point $\Delta\theta = -\pi/2$. The output power decreases with V_1 but increases with V_2 since the corresponding signal lines are in the opposite arm of the MZI (see Fig. 1(b)). Therefore, the electrical Gaussian pulse applied to the segment-1 generates a negative Gaussian pulse. On the contrary, the electrical pulse on segment-2 generates a positive Gaussian pulse. By adjusting the relative time delay between the two generated optical Gaussian pulses, a UWB pulse is generated.

From Eq. (1), we observe that the phase of E_{out} is $2\pi f_c t + \varphi_1 + \varphi_2 + \Delta\theta/2$, where $\Delta\theta$ is fixed for a certain operating point, φ_1 and φ_2 are also fixed when the DC bias voltages are set. It indicates the instantaneous frequency of the generated signal is fixed at f_c, and therefore the generated monocycle pulse is chirp-free.

4. Characterization of the SMZM

We first measured the transmission spectra of the SMZM when different bias voltages were applied on one PN junction of segment-1 and segment-2. Figs. 5(a) and 5(b) show the results. The device fiber-to-fiber insertion loss is about 12.6 dB at 0-V bias. The loss consists of 5 dB coupling loss (2.5 dB/facet) and 7.6 dB on-chip loss including passive waveguide loss and doping-induced absorption loss. The coupling loss can be reduced by optimizing the fiber-to-waveguide mode conversion structure [39]. The doping loss can be reduced by lowering the doping concentrations

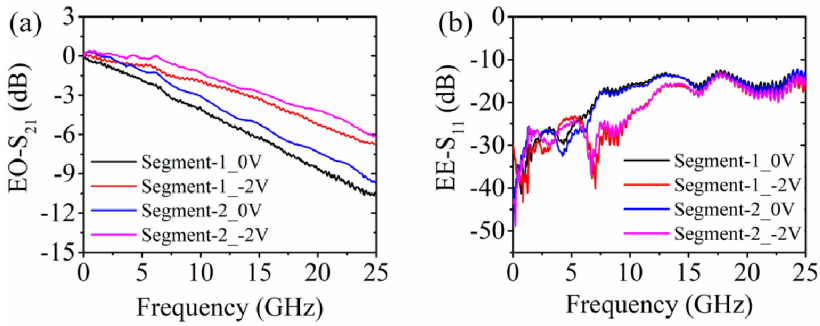

Fig. 6. Small-signal (a) electro-optic (EO) S_{21} and (b) electro-electro (EE) S_{11} responses of segment-1 and segment-2 at 0 V and −2 V DC biases.

of the PN junctions and shortening the active arm length, but with the sacrifice of modulation efficiency. Fig. 5(c) shows the extracted phase shift as a function of bias voltage. The half-wave voltage is about 8 V for both segments. The small-signal modulation efficiency, measured by the product of half-wave voltage and active arm length ($V\pi \cdot L$), is about 1.39 V·cm and 1.31 V·cm for segment-1 and segment-2 at −1 V bias, respectively. The slight difference in modulation efficiency between two segments may be caused by the fabrication error-induced non-uniformity.

Then, we used a 43.5-GHz vector network analyzer (VNA, Keysight, N5224A) and a 50 GHz photodiode (PD, U2t, XPVD2120R) to characterize the microwave response of the two segments. The light wavelength was set at 1551.7 nm, which is the quadrature point of this modulator. Fig. 6(a) shows the EO-S_{21} response of segment-1 and segment-2 at 0 V and −2 V biases. The EO-S_{21} curve was normalized to the 100 MHz frequency point. The 3-dB EO bandwidth of segment-1/segment-2 is about 14.1/15.7 GHz at −2 V bias. Fig. 6(b) shows the EE-S_{11} responses of the two segments. The RF reflection is below −10 dB from 100 MHz to 25 GHz, indicating a good impedance match and thus small reflection from the modulator. The non-identical microwave responses of the two segments may be caused by the fabrication error-induced non-uniformity. It will result in a slight difference between the peak and the trough of the generated UWB signal.

5. UWB Generation Setup and Results

Fig. 7 shows the experimental setup for generating the UWB pulses. Two pulse pattern generators (PPG, Keysight, N4960A and N4951B) generate two independent Gaussian-like pulse streams with the data pattern being 1 '0' bit and 31 '1' bits at a bit rate of 20 Gb/s. Thus, the repetition rate of the pulse train is 625 MHz and the duty cycle is 1/32. The time delay between the two pulse trains can be adjusted by the controller (Keysight, N4960A). The pulses had a peak-to-peak voltage (V_{pp}) of 3 V and were applied to the SMZM through a 40-GHz GSGSG microwave probe. The pulse pattern possessing a single 0 followed by many 1's could be regarded as a Gaussian-like pulse with the amplitude being –3 V (inverted Gaussian pulse). The driving voltage of the electrical Gaussian-like pulse should not be larger than the $V_\pi/2$ of the modulator. Therefore, when $\Delta\theta = -\pi/2$ and $\pi/2$, positive and negative monocycle pulses are generated, respectively. The other ends of the segments were terminated with two external 50-ohm resistors through another 40-GHz GSGSG microwave probe. Light generated from a tunable laser source was set to the transverse electric (TE) polarization and coupled to the modulator through a lens fiber. The modulated optical waveform was amplified by an erbium-doped optical amplifier (EDFA) and filtered by a tunable optical band-pass filter. The optical bandwidth of the filter is set at 1 nm. The electrical signal detected by the 50-GHz photodiode (PD, U^2t, XPDV2120R) was divided into two branches through a microwave splitter. One branch was sent to the digital communication analyzer (DCA, Agilent, DCA-X 86100D) to measure the temporal shape of the generated UWB signal. Another branch

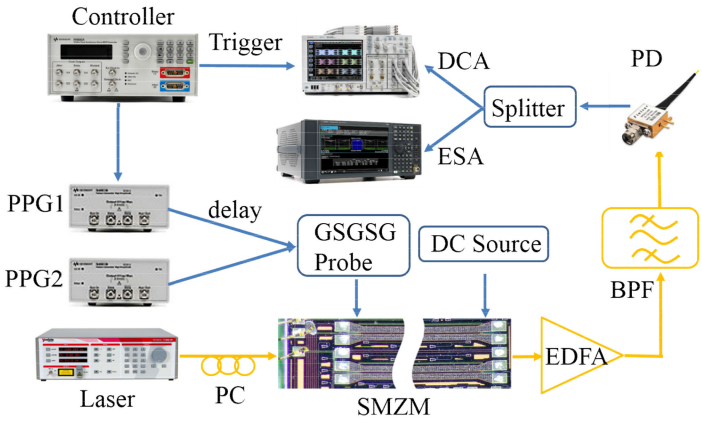

Fig. 7. Experimental setup for UWB pulse generation using the SMZM. PPG: pulse pattern generator; PC: polarization controller; EDFA: erbium-doped fiber amplifier; BPF: band-pass filter; PD: photodiode; DCA: digital communication analyzer; ESA: electrical spectrum analyzer. The yellow arrows indicate the optical paths. The blue arrows indicate the electrical paths.

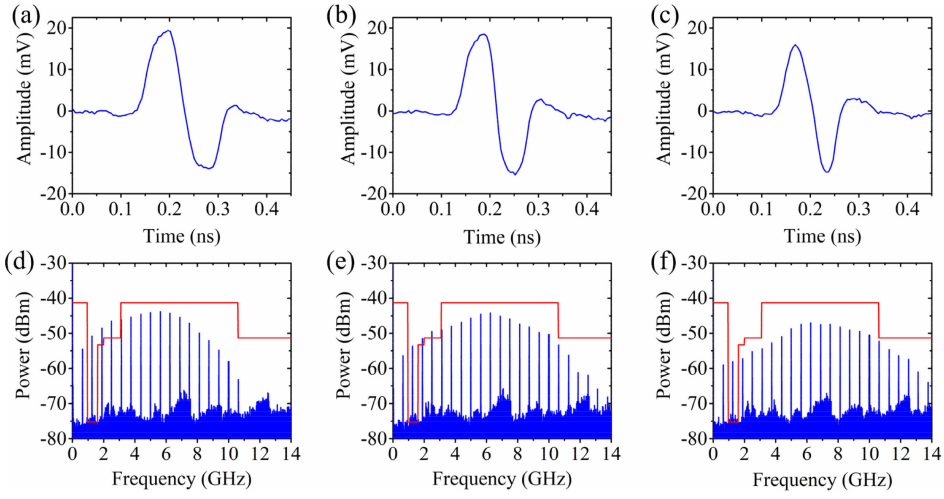

Fig. 8. (a–c) Temporal waveforms and (d–f) corresponding electrical spectra of the generated positive monocycle UWB pulses with a relative time delay of (a, d) 81 ps, (b, e) 56 ps, and (c, f) 31 ps. The red lines in the electrical spectra are the FCC mask.

was sent to the electrical spectrum analyzer (ESA, Keysight, N9000B) to analyze its spectrum simultaneously. The DC bias voltages of this modulator were applied through the PCB to ensure PN junctions of the modulator to work in the carrier-depletion condition. The DC bias voltages V_{d1} and V_{d2} of the two segments were both set to 2 V. The power of the laser is set at 10 dBm and the average optical power of received by the PD is about 5 dBm by adjusting the EDFA gain.

We set the light wavelength at 1551.7 nm, which is the quadrature point of this modulator ($\Delta\theta = -\pi/2$). Fig. 8 shows the waveforms and electrical spectra for different time delays between the Gaussian-like pulses. Table 1 shows the performance specifications of the generated positive monocycle UWB pulses for three relative time delay values. With a shorter time delay, the amplitude of the generated UWB signal decreases, the FWHM of the peak and trough decreases, the center frequency of the UWB pulses increases, and the 10-dB bandwidth becomes broader, leading to an overall decreased fractional bandwidth. The peak and trough of the generated UWB signal are slightly different. This is mainly due to the imperfection in the electrical driving pulse from the PPG,

TABLE 1
Performance Specifications of the Generated UWB Signal With Different Relative Time Delays

Time delay (ps)	Peak FWHM (ps)	Trough FWHM (ps)	10-dB bandwidth (GHz)	Center frequency (GHz)	Fractional bandwidth (%)
81	64.5	62.5	8.37	4.95	169
56	58.3	54.4	9.64	5.97	161
31	44.9	37.8	10.26	7.10	145

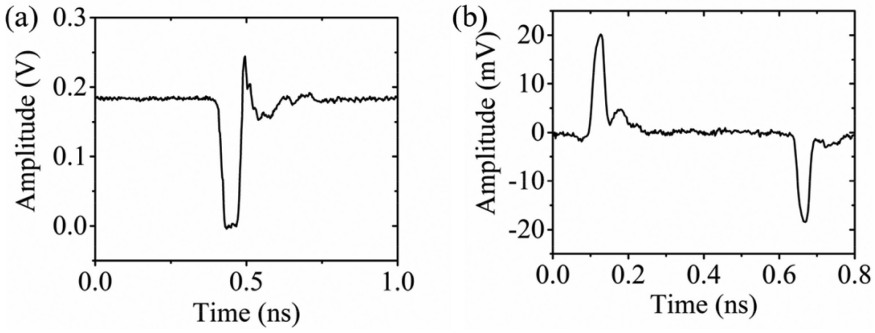

Fig. 9. (a) Electrical driving pulse from the PPG with the data pattern being 1 '0' bit and 31 '1' bits at a bit rate of 20 Gb/s. (b) Generated Gaussian-like pulses of opposite polarities in the optical domain. The relative time delay between the two pulses is 0.54 ns. The optical wavelength is set at 1551.7 nm.

as shown in Fig. 9(a). After modulation, a small peak follows the primary Gaussian-like pulse in the optical domain, as shown in Fig. 9(b). When two pulses of opposite polarities are combined to form the UWB signal, the presence of the small peak produces the difference between the peak and the trough.

Then, we fixed the time delay at 56 ps while changed the optical wavelength to investigate its impact on the UWB pulse waveform and the RF spectrum. Fig. 10 shows the results for two other wavelengths. When the wavelength was 1553.3 nm, the SMZM worked at the carrier suppression point ($\Delta\theta = \pi$). The monocycle UWB pulse cannot be generated. Instead, double-peak pulses were generated since both segments produced positive pulses. When the optical wavelength was 1554.9 nm, the SMZM worked at the other quadrature point ($\Delta\theta = \pi/2$). Negative monocycle UWB pulses were generated, which is opposite to those in Fig. 8. The FWHM of the trough and peak is 58.7 ps and 53.3 ps, respectively. The center frequency is about 6.02 GHz and the 10-dB bandwidth is about 9.89 GHz (from 1.08 GHz to 10.97 GHz). Thus, the fractional bandwidth is 164%. Therefore, it indicates that the generation of UWB pulses is quite dependent on the operating point of the SMZM. Note that the RF spectrum of the generated UWB monocycle signals fulfills the Federal Communications Commission (FCC) mask requirement. However, there is infringement in the global positioning system (GPS) band (from 0.96 GHz to 1.61 GHz). These unwanted RF frequencies could be filtered by a UWB antenna [4]. We simulated the power spectrum of the generated UWB signal after it was filtered by a UWB antenna. In our simulation, we adopt the frequency response of the UWB antennas pair with a distance of 1 cm [4]. Figs. 11(a) and 11(b) show the simulated spectra when the optical wavelength is set at 1551.7 nm and 1554.9 nm, respectively. It reveals that the RF frequency components in the GPS band are removed by the UWB antenna and the 10-dB bandwidth of the UWB signal is decreased. The center frequency is about 6.25 GHz and the 10-dB bandwidth is about 6.71 GHz (from 2.89 GHz to 9.6 GHz) in Fig. 11(a). Thus, the fractional bandwidth is 107%. The center frequency is about 6.2 GHz and the 10-dB bandwidth is about 6.8 GHz (from 2.80 GHz to 9.6 GHz) in Fig. 11(b). Thus, the fractional bandwidth is 110%. In the future, we could use an SMZM with a low V_π [40, 41] to produce high-order UWB signals following the method adopted in [36].

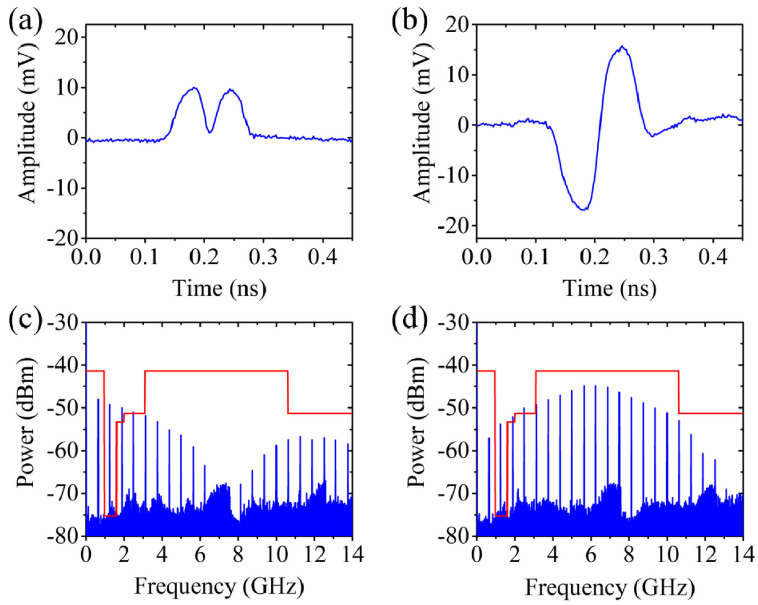

Fig. 10. (a, b) Temporal waveforms and (c, d) corresponding electrical spectra when the optical wavelength is tuned to (a, c) 1553.3 nm and (b, d) 1554.9 nm.

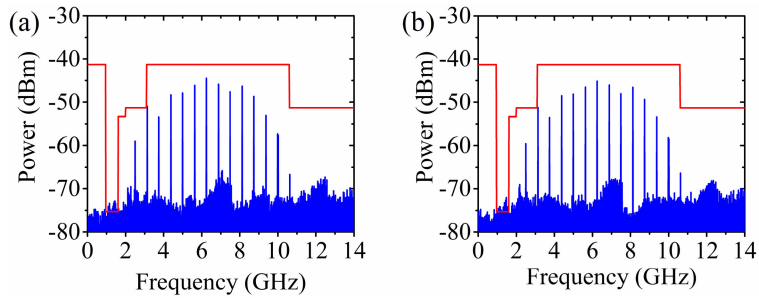

Fig. 11. UWB signal electrical spectra with the GPS band eliminated by a UWB antenna when the optical wavelength is set at (a) 1551.7 nm and (b) 1554.9 nm and the relative time delay is 56 ps.

Finally, we also demonstrated digital data modulation on the UWB pulse train. By coding the RF driving signal, the UWB pulses can be modulated with on-off keying (OOK) and pulse position modulation (PPM) formats. We set the input 625-Mb/s data to a fixed pattern of “1110010”. Fig. 12(a) shows the waveform of the generated positive monocycle signal with OOK modulation. We could see that the monocycle is present at the “1” bit while absent at the “0” bit. The corresponding electrical spectrum is shown in Fig. 12(b). For PPM, there is a time shift between the “0” bit and “1” bit of the generated monocycle pulses. For orthogonal pulse position modulation (OPPM), the time shift is equal to a half bit. Otherwise, it is nonorthogonal pulse position modulation (NPPM). Figs. 12(c) and 12(e) show the waveforms of the generated positive monocycle signals with NPPM and OPPM, respectively. Figs. 12(d) and 12(f) show the corresponding electrical spectra. The time shift is about 0.4 ns in the NPPM and 0.8 ns in the OPPM. These results indicate that modulating the UWB signal with OOK and PPM formats is feasible by simply coding the electrical driving signal.

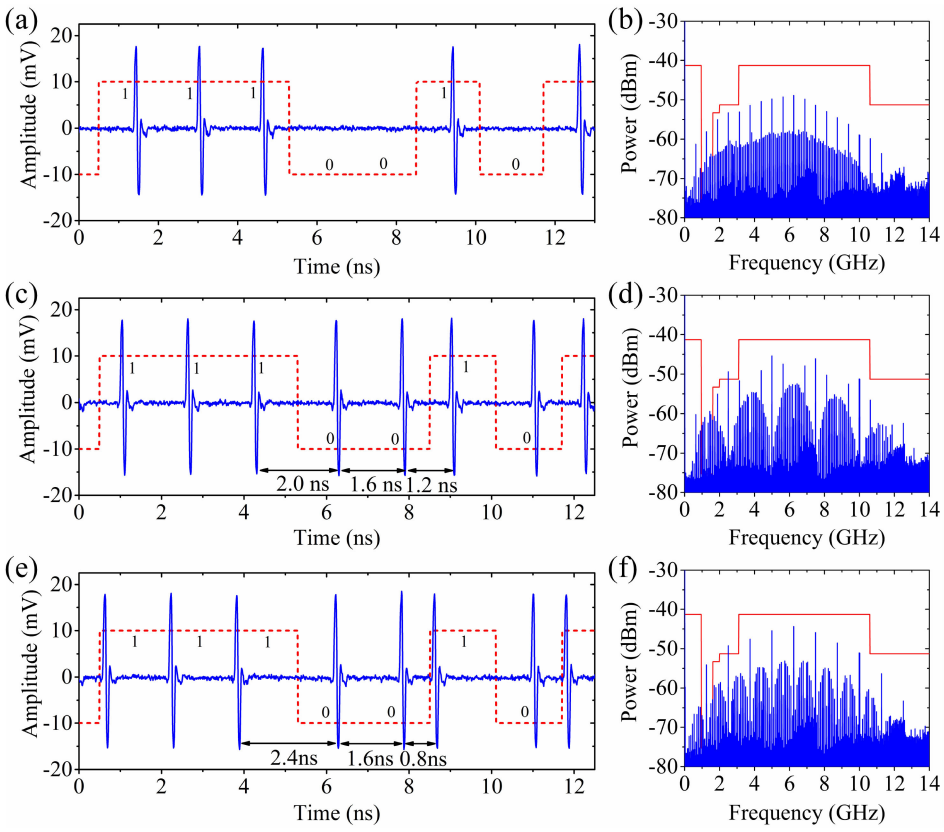

Fig. 12. (a, c, e) Waveforms and (d–f) corresponding electrical spectra of the modulated UWB signal with (a, b) OOK, (c, d) NPPM, (e, f) OPPM formats. The data pattern of the driving signal is "1110010" outlined by the red dotted lines.

6. Chirp Characterization

Due to the limit of the instrument, we cannot directly measure the instantaneous frequency of the generated optical UWB signal. Instead, we measured the chirp parameter (α) of the SMZM, which is defined as [42]:

$$\alpha_{chirp} = 2I(d\phi/dt)/(dI/dt) \tag{12}$$

where I and ϕ are the instantaneous intensity and phase of the optical signal, respectively. Chirp is free when $\alpha = 0$. We used the fiber response peak method to measure the chirp of the SMZM [43]. Fig. 13 shows the experimental setup. The input light with 10 dBm optical power is modulated by the SMZM driven by a 20-GHz vector network analyzer (VNA, Keysight, E5071C) with 3 dBm RF power. The DC bias voltages of the two segments are both set at 2 V. The modulated optical signal passes a 50 km single-mode fiber working as the dispersive medium. It is amplified to 0 dBm average power by adjusting the EDFA gain and detected by a 50-GHz PD. The detected signal is received by the VNA to get the S_{21} response of the system. The resonance frequency f_u in the S_{21} response is expressed as

$$f_u^2 = \frac{c}{2DL\lambda^2}\left(1 + 2u - \frac{2}{\pi}\arctan(\alpha)\right) \tag{13}$$

where c is the light velocity in vacuum, L is the fiber length, D is the fiber dispersion, λ is the optical wavelength, and u is the order of the resonance.

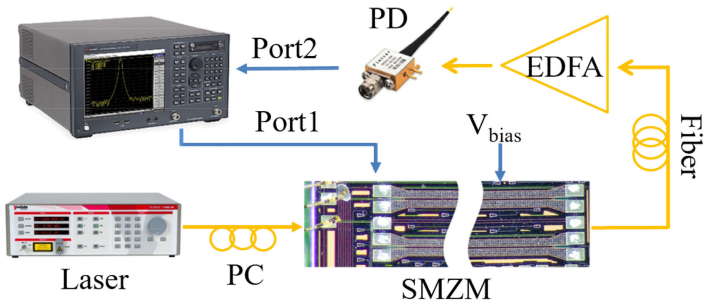

Fig. 13. Experimental setup for chirp characterization of the SMZM.

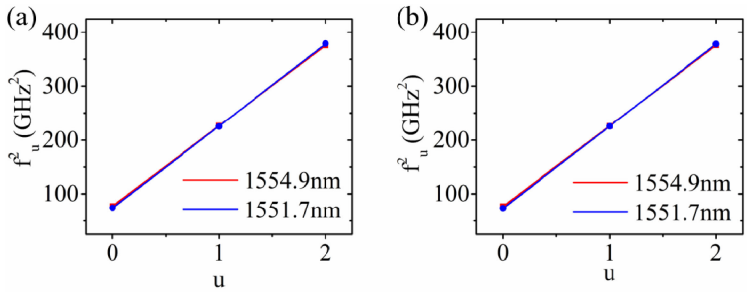

Fig. 14. Resonance frequency squared as a function of the order of the resonance for (a) segment-1 and (b) segment-2 at 2 V bias. The dots represent the measured data and the straight lines are linear fitting.

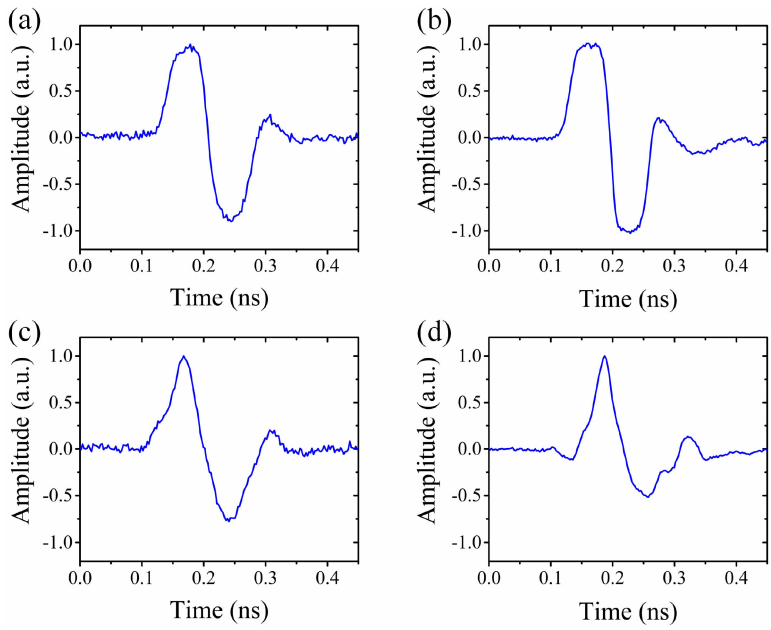

Fig. 15. Waveform of the generated UWB signal after (a, b) B2B transmission and (c, d) 30-km fiber transmission. (a, c) presents the results from the SMZM and (b, d) from a commercial LN dual-drive modulator.

Fig. 14 shows the measured resonance frequency squared as a function of the order of resonance for segment-1 and segment-2. According to (13), the retrieved chirp parameter is 0.056 (-0.055) for segment-1 and 0.064 (-0.0546) for segment-2 when the wavelength is set at 1551.7 nm (1554.9 nm). The residual chirp could be caused by the FCD and FCA effects in silicon [44], [45]. Besides, the finite interference extinction ratio due to the slight imbalance between the two arms of the modulator could also lead to residual chirp [42]. For comparison, we measured the chirp of a commercial LN dual-drive modulator (T.DEH1.5-40PD-ADC) under a single drive condition using the same method. The operating point is set at the quadrature point of the modulator. The measured α is -1.070 and 0.984 when either one of the arms is modulated. The chirp parameter measurement proves that the SMZM has more than one order lower chirp than the LN dual-drive modulator under a single drive condition. Therefore, it indicates that the chirp of our SMZM is reduced considerably and the generated UWB signal has much a lower chirp than that generated by the dual-drive LN modulator [17], [36]. We also measured the waveform of the generated UWB signal using our device and a commercial LN dual-drive modulator after B2B transmission and 30-km fiber transmission, as shown in Fig. 15. After 30-km fiber transmission, the UWB signal generated in our device still has relatively good symmetry. However, the UWB signal generated by the LN dual-drive modulator is distorted considerably. This is because the UWB signal generated by the LN dual-drive modulator is highly chirped [17]. Thus, it indicates that the UWB signal generated using the SMZM has relatively good tolerance to the CD of the optical fiber.

7. Conclusions

We have presented an approach to generate low-chirp UWB signals based on a silicon SMZM. Both positive- and negative-polarity monocycle pulses can be generated by driving the modulator at the quadrature operating point by two Gaussian-like pulses with a relative delay. We investigated the influence of time delay and optical wavelength on the UWB pulses. When the relative time delay is 56 ps, the center frequency of the generated negative and positive monocycle pulses is 5.97 GHz and 6.02 GHz with a 161% and 164% fractional bandwidth, respectively. By coding the applied signal, the UWB signal can be modulated with OOK and PPM formats. Owning to the push-pull driving scheme, the generated UWB signal has low chirps. The residual chirp is due to the nonlinear FCD and FCA effects in silicon and the finite extinction ratio of the MZI. To get a positive or negative UWB pulse, we should set the operating point of the MZM at the quadrature point ($\Delta\theta = -\pi/2$ or $\Delta\theta = \pi/2$). Our modulator is based on an imbalanced MZI structure and the arm length difference is 90 um. Therefore, we can change the operating point of the MZM by changing the optical wavelength. At certain wavelengths that satisfy the quadrature operating point, UWB pulses can be generated. If we adopted a balanced MZI structure, then a thermo-optic phase shifter could be used to change the operating point. Besides, the generated UWB would be insensitive to the environmental temperature [40]. The successful generation of UWB signals using our silicon SMZM poses a significant step in realizing a compact low-cost and low-chirp UWB generator on the silicon photonics platform for UWB wireless communications.

References

[1] G. R. Aiello and G. D. Rogerson, "Ultra-wideband wireless systems," *IEEE Microw. Mag.*, vol. 4, no. 2, pp. 36–47, Jun. 2003.
[2] D. Porcino and W. Hirt, "Ultra-wideband radio technology: Potential and challenges ahead," *IEEE Commun. Mag.*, vol. 41, no. 7, pp. 66–74, Jul. 2003.
[3] C. M. Tan, L. C. Ong, M. L. Yee, B. Luo, and P. K. Tang, "Direct transmission of ultra wide band signals using single mode radio-over-fiber system," in *Proc. Asia-Pacific Microw. Conf.*, vol. 2, p. 3, Dec. 2005.
[4] S. Pan and J. Yao, "UWB-over-fiber communications: Modulation and transmission," *J. Lightw. Technol.*, vol. 28, no. 16, pp. 2445–2455, Aug. 2010.
[5] J. Yao, F. Zeng, and Q. Wang, "Photonic generation of ultrawideband signals," *J. Lightw. Technol.*, vol. 25, no. 11, pp. 3219–3235, Nov. 2007.

[6] F. Zeng and J. Yao, "Ultrawideband impulse radio signal generation using a high-speed electrooptic phase modulator and a fiber-bragg-grating-based frequency discriminator," *IEEE Photon. Technol. Lett.*, vol. 18, no. 19, pp. 2062–2064, Oct. 2006.

[7] J. Li *et al.*, "Photonic polarity-switchable ultra-wideband pulse generation using a tunable sagnac interferometer comb filter," *IEEE Photon. Technol. Lett.*, vol. 20, no. 15, pp. 1320–1322, Aug. 2008.

[8] S. Pan and J. Yao, "Switchable UWB pulse generation using a phase modulator and a reconfigurable asymmetric Mach–Zehnder interferometer," *Opt. Lett.*, vol. 34, no. 2, pp. 160–162, Jan. 2009.

[9] F. Liu, T. Wang, Z. Zhang, M. Qiu, and Y. Su, "On-chip photonic generation of ultra-wideband monocycle pulses," *Electron. Lett.*, vol. 45, no. 24, pp. 1247–1249, Nov. 2009.

[10] K. Xu *et al.*, "Amplitude and phase modulation of uwb monocycle pulses on a silicon photonic chip," *IEEE Photon. Technol. Lett.*, vol. 28, no. 3, pp. 248–251, Feb. 2016.

[11] D. Marpaung, L. Chevalier, M. Burla, and C. Roeloffzen, "Impulse radio ultrawideband pulse shaper based on a programmable photonic chip frequency discriminator," *Opt. Express*, vol. 19, no. 25, pp. 24838–24848, Dec. 2011.

[12] J. Dong, X. Zhang, J. Xu, and D. Huang, "All-optical ultrawideband monocycle generation utilizing gain saturation of a dark return-to-zero signal in a semiconductor optical amplifier," *Opt. Lett.*, vol. 32, no. 15, pp. 2158–2160, Aug. 2007.

[13] J. Dong, X. Zhang, J. Xu, D. Huang, S. Fu, and P. Shum, "Ultrawideband monocycle generation using cross-phase modulation in a semiconductor optical amplifier," *Opt. Lett.*, vol. 32, no. 10, pp. 1223–1225, May 2007.

[14] Q. Wang, F. Zeng, S. Blais, and J. Yao, "Optical ultrawideband monocycle pulse generation based on cross-gain modulation in a semiconductor optical amplifier," *Opt. Lett.*, vol. 31, no. 21, pp. 3083–3085, Nov. 2006.

[15] M. Bolea, J. Mora, B. Ortega, and J. Capmany, "Optical UWB pulse generator using an n tap microwave photonic filter and phase inversion adaptable to different pulse modulation formats," *Opt. Express*, vol. 17, no. 7, pp. 5023–5032, Mar. 2009.

[16] J. Li *et al.*, "Photonic ultrawideband monocycle pulse generation using a single electro-optic modulator," *Opt. Lett.*, vol. 33, no. 3, pp. 288–290, Feb. 2008.

[17] S. Pan and J. Yao, "Performance evaluation of UWB signal transmission over optical fiber," *IEEE J. Sel. Area Commun.*, vol. 28, no. 6, pp. 889–900, Aug. 2010.

[18] H. Chen, M. Chen, C. Qiu, J. Zhang, and S. Xie, "UWB monocycle pulse generation by optical polarisation time delay method," *Electron. Lett.*, vol. 43, no. 9, pp. 542–543, Apr. 2007.

[19] Q. Wang and J. Yao, "Switchable optical UWB monocycle and doublet generation using a reconfigurable photonic microwave delay-line filter," *Opt. Express*, vol. 15, no. 22, pp. 14667–14672, Oct. 2007.

[20] Y. Yu, J. Dong, X. Li, and X. Zhang, "Ultra-wideband generation based on cascaded Mach–Zehnder modulators," *IEEE Photon. Technol. Lett.*, vol. 23, no. 23, pp. 1754–1756, Dec. 2011.

[21] D. Marpaung, J. Yao, and J. Capmany, "Integrated microwave photonics," *Nat. Photon.*, vol. 13, no. 2, pp. 80–90, Feb. 2019.

[22] C. G. H. Roeloffzen *et al.*, "Silicon nitride microwave photonic circuits," *Opt. Express*, vol. 21, no. 19, pp. 22937–22961, Sept. 2013.

[23] L. M. Augustin *et al.*, "InP-based generic foundry platform for photonic integrated circuits," *IEEE J. Sel. Topics Quantum Electron.*, vol. 24, Jan./Feb. 2018, Art. no. 6100210.

[24] W. Zhang and J. Yao, "Silicon-based integrated microwave photonics," *IEEE J. Quantum Electron.*, vol. 52, no. 1, pp. 1–12, Jan. 2016.

[25] Y. Zhou, L. Zhou, F. Su, X. Li, and J. Chen, "Linearity measurement and pulse amplitude modulation in a silicon single-drive push–pull Mach–Zehnder modulator," *J. Lightw. Technol.*, vol. 34, no. 14, pp. 3323–3329, Jul. 2016.

[26] M. Li, L. Wang, X. Li, X. Xiao, and S. Yu, "Silicon intensity Mach–Zehnder modulator for single lane 100 Gb/s applications," *Photon. Res.*, vol. 6, no. 2, pp. 109–116, Feb. 2018.

[27] J. Sun, R. Kumar, M. Sakib, J. B. Driscoll, H. Jayatilleka, and H. Rong, "A 128 Gb/s PAM4 silicon microring modulator with integrated thermo-optic resonance tuning," *J. Lightw. Technol.*, vol. 37, no. 1, pp. 110–115, Jan. 2019.

[28] W. Zhang and J. Yao, "On-chip silicon photonic integrated frequency-tunable bandpass microwave photonic filter," *Opt. Lett.*, vol. 43, no. 15, pp. 3622–3625, Aug. 2018.

[29] W. Zhang and J. Yao, "Silicon photonic integrated optoelectronic oscillator for frequency-tunable microwave generation," *J. Lightw. Technol.*, vol. 36, no. 19, pp. 4655–4663, Oct. 2018.

[30] I. Demirtzioglou *et al.*, "Frequency comb generation in a silicon ring resonator modulator," *Opt. Express*, vol. 26, no. 2, pp. 790–796, Jan. 2018.

[31] S. Liu *et al.*, "Optical frequency comb and nyquist pulse generation with integrated silicon modulators," *IEEE J. Sel. Topics Quantum Electron.*, vol. 26, no. 2, pp. 1–8, Mar./Apr. 2020.

[32] Y. Xie, L. Zhuang, and A. J. Lowery, "Silicon microring modulator-based RF mixer for millimeter-wave phase-coded signal generation," *Opt. Lett.*, vol. 42, no. 14, pp. 2742–2745, Jul. 2017.

[33] Z. Xu, L. Zhou, S. Chen, G. Zhou, L. Lu, and J. Chen, "UWB pulses generation with fano resonance modulation," in *Proc. Int. Topical Meeting Microw. Photon.*, Oct. 2019, pp. 1–3.

[34] A. Samani *et al.*, "Experimental parametric study of 128 Gb/s PAM-4 transmission system using a multi-electrode silicon photonic Mach–Zehnder modulator," *Opt. Express*, vol. 25, no. 12, pp. 13252–13262, Jun. 2017.

[35] G. Zhou, L. Zhou, L. Lu, Y. Guo, and J. Chen, "Phase-coded microwave signal generation based on a segmented silicon Mach–Zehnder modulator," *IEEE J. Sel. Topics Quantum Electron.*, vol. 26, no. 2, pp. 1–8, Mar./Apr. 2020.

[36] P. Cao, X. Hu, J. Wu, L. Zhang, X. Jiang, and Y. Su, "Reconfigurable UWB pulse generation based on a dual-drive Mach–Zehnder modulator," *IEEE Photon. J.*, vol. 6, no. 5, Oct. 2014, Art. no. 7903206.

[37] L. Chen, C. R. Doerr, P. Dong, and Y.-K. Chen, "Monolithic silicon chip with 10 modulator channels at 25 gbps and 100-GHz spacing," *Opt. Express*, vol. 19, no. 26, pp. B946–B951, Dec. 2011.

[38] N.-N. Feng *et al.*, "High speed carrier-depletion modulators with 1.4 V-cm v π l integrated on 0.25 μm silicon-on-insulator waveguides," *Opt. Express*, vol. 18, no. 8, pp. 7994–7999, Apr. 2010.

[39] L. Jia, C. Li, T.-Y. Liow, and G.-Q. Lo, "Efficient suspended coupler with loss less than -1.4 dB between si-photonic waveguide and cleaved single mode fiber," *J. Lightw. Technol.*, vol. 36, no. 2, pp. 239–244, Jan. 2018.

[40] K. Goi *et al*., "Low-voltage silicon Mach–Zehnder modulator operating at high temperatures without thermo-electric cooling," in *Proc. Opt. Fiber Commun. Conf.*, Mar. 2016, Art. no. W2A.23.
[41] G. Zhou *et al*., "32-Gb/s OOK and 64-Gb/s PAM-4 modulation using a single-drive silicon Mach–Zehnder modulator with 2 v drive voltage," *IEEE Photon. J.*, vol. 11, no. 6, Dec. 2019, Art. no. 6603610.
[42] K. Hoon and A. H. Gnauck, "Chirp characteristics of dual-drive. Mach–Zehnder modulator with a finite DC extinction ratio," *IEEE Photon. Technol. Lett.*, vol. 14, no. 3, pp. 298–300, Mar. 2002.
[43] F. Devaux, Y. Sorel, and J. F. Kerdiles, "Simple measurement of fiber dispersion and of chirp parameter of intensity modulated light emitter," *J. Lightw. Technol.*, vol. 11, no. 12, pp. 1937–1940, Dec. 1993.
[44] H. Shao, W. Chen, Y. Zhao, H. Chi, J. Yang, and X. Jiang, "Performance evaluation of photonic UWB generation based on silicon MZM," *Opt. Express*, vol. 20, no. 7, pp. 7398–7403, Mar. 2012.
[45] Y. Wei, Y. Zhao, J. Yang, M. Wang, and X. Jiang, "Chirp characteristics of silicon Mach–Zehnder modulator under small-signal modulation," *J. Lightw. Technol.*, vol. 29, no. 7, pp. 1011–1017, Apr. 2011.